

ASEN 2002 - Lab 4

Jack Isbill, *

Benjamin Vidaurre, † Ginger Beerman, ‡ Nicholas Renninger, §

University of Colorado - Boulder

This report details the process for determining the aerodynamic forces on a cambered Clark Y-14 airfoil as angle of attack and free-stream airspeed varies. With the knowledge that all aerodynamic forces stem from pressure and shear-stress distributions along the airfoil, the lift and drag on the airfoil are identified by integrating the pressure distribution around the airfoil. To show how aerodynamic forces vary with angle of attack and airspeed, the pressure distribution along the airfoil was measured as flow conditions were varied with respect to both the angle of attack and the flow velocity. The airfoil was measured to produce a maximum lift coefficient of 1.376 at an angle of attack of 11 degrees. Stall occurred on the airfoil most readily at 10 [m/s], and the airfoil was most resistive to stall and flow separation at a velocity of 30 [m/s]. Flow separation occurred early chord-wise on the airfoil, and thus the airfoil showed leading edge stall characteristics. All of this data was compared to previous measurements of the Clark Y-14 airfoil geometry taken by NACA in 1938, and the experimental data taken in this lab was found to match very well with this NACA data. The largest differences between the experimental and NACA reference data were attributed to the different Reynolds numbers used in testing, and the difference in pressure measurement techniques used.

Nomenclature

α	= Angle of Attack ($^{\circ}$)
c	= Chord Length (m)
C_d	= Coefficient of Drag
C_l	= Coefficient of Lift
C_p	= Coefficient of Pressure
p	= Pressure at scanivalve port on Airfoil (Pa)
p_{∞}	= Free-Stream Pressure (Pa)
q_{∞}	= Dynamic Pressure (Pa)
V	= Velocity over airfoil surface (m/s)
V_{∞}	= Free-Stream Velocity (m/s)
x	= x position along airfoil, shown in Figure 1 (in)
y	= y position along airfoil, shown in Figure 1 (in)

I. Introduction

The principle axiom for flight, powered or unpowered, is the relationship between lift and drag on an aircraft. Practically, such quantities are not inherently defined as pressure or temperature are. As such,

*103222853

†104286050

‡104773020

§105492876

analysis of the pressure distribution over the airfoil must be done in order to be able to quantify the lift and drag for a particular angle of attack. The pressure is measured using an airfoil with integrated static ports along its profile, allowing for a differential pressure reading relative to the free-stream static pressure to be determined at each port. These pressures can then be used to determine the lift and drag on the airfoil. Using pressure measurements taken with varied wind speeds and angles of attack, the effects of the angle of attack and wind speed on lift and drag can be examined.

II. Experimental Setup and Measurement Techniques

The measurement configuration for the gathering of the pressure data consisted of an Clark Y-14 airfoil with integrated pressure sensors, a static ring for the determination of the free stream static pressure, and a pitot tube to determine q_∞ . The airfoil has 19 co-planar static ports, 3 of which are not measured by the Scanivalve system as seen in Figure 1. The trailing edge of the airfoil cannot effectively be measured by a static port (blue port on Figure 1), requiring the surrounding ports to facilitate an extrapolation of the pressure at the trailing edge to establish a comprehensive pressure profile. Each of the measurements taken at a particular static port are related to the free stream static pressure, as measured by the static ring at the entrance of the test section, and expressed as a differential pressure. These pressures are then used to approximate the axial and normal force coefficients, which are directly relatable to the lift and drag coefficients for the particular conditions.

This group measured data for angles of attack of -7, 3, and 13 degrees at wind speeds of 10, 20, and 30 [m/s]. Other groups measured data at other various angles of attack which allowed for data over a complete range of angles from -14 to 15 degrees to be analyzed.

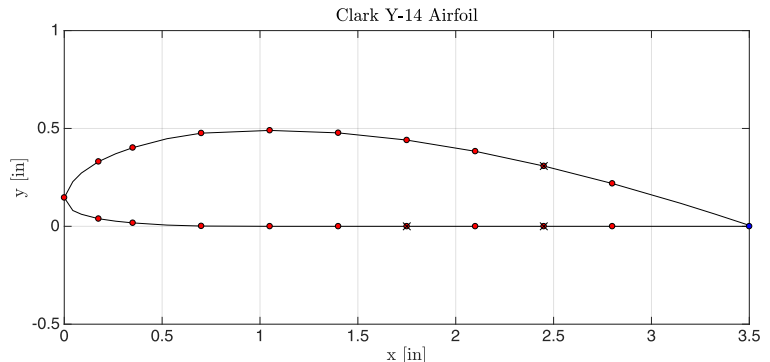


Figure 1: Profile of Clark Y-14 airfoil showing x and y coordinates of pressure ports, which ports are active, and the theoretical trailing edge port

III. Post-Processing and Calculation of Force Coefficients

Using MATLAB, post processing of raw measurements began by organizing and averaging the data obtained by the LAs of the class in the wind tunnel. Data was organized so that static pressure at each port, flow pressure and dynamic pressure could be obtained easily for any angle of attack between -14 and 15 degrees and at either 10, 20, or 30 [m/s] flow velocity.

At this point the pressure coefficient for all upper and lower points could be found and plotted using equation (1), however it was necessary to extrapolate the pressure coefficient at the trailing edge of the airfoil to complete the data set. Following this process the team was then able to perform the appropriate integration to obtain lift and drag coefficients for each data set. This integration was carried out using the following formulas for the numeric integration needed to calculate the normal and axial coefficients:

$$C_n = - \sum_{i=1}^n \frac{1}{2} (C_{p,i} + C_{p,i+1}) \frac{\Delta x_i}{c} \quad (1)$$

$$C_a = \sum_{i=1}^n \frac{1}{2} (C_{p,i} + C_{p,i+1}) \frac{\Delta y_i}{c} \quad (2)$$

where Δx_i and Δy_i are defined as follows:

$$\Delta x_i = x_{i+1} - x_i, \quad \Delta y_i = y_{i+1} - y_i \quad (3)$$

There are many uncertainties that are valid to account for in the process of obtaining lift and drag coefficients in this lab. The most major source of uncertainty in this lab is the uncertainty propagated from

the pressure measurement devices which affects all the pressure ports' data. More specifically, the Scanivalve differential pressure measurement device contributes the most to the uncertainties in the calculation of C_l and C_d . This is due to the full-range error of 0.2% as quoted by the manufacturer. Due to the fact that this error is full-range, as the velocities and thus the pressures in the tunnel decrease, the uncertainty in the differential pressure measurement becomes large. This happens as the measured pressure becomes smaller; the error is constant and thus becomes a larger percentage of the measurement. The uncertainty which is propagated from the extrapolation process only affects one of the 17 pressure port data points and thus is much less influential.

The estimate of the trailing edge pressure coefficient is most likely only moderately accurate, however as discussed above, it is not nearly as influential as the combined pressure data obtained at all other pressure ports.

IV. Airfoil Static Pressure Coefficient Distribution

To further understand how flow conditions affect the pressure distribution over an airfoil, the pressure coefficient, C_p , was plotted against the normalized chord-wise position, $\frac{x}{c}$. The coefficient of pressure is defined in Equation 4.

$$C_p = \frac{p - p_\infty}{\frac{1}{2}\rho_\infty V_\infty^2} = \frac{p - p_\infty}{q_\infty} \quad (4)$$

When relating the local speeds at different locations along the airfoil to the pressure coefficient, Bernoulli's equation is used resulting in Equation 5:

$$C_p = 1 - \frac{V^2}{V_\infty^2} \quad (5)$$

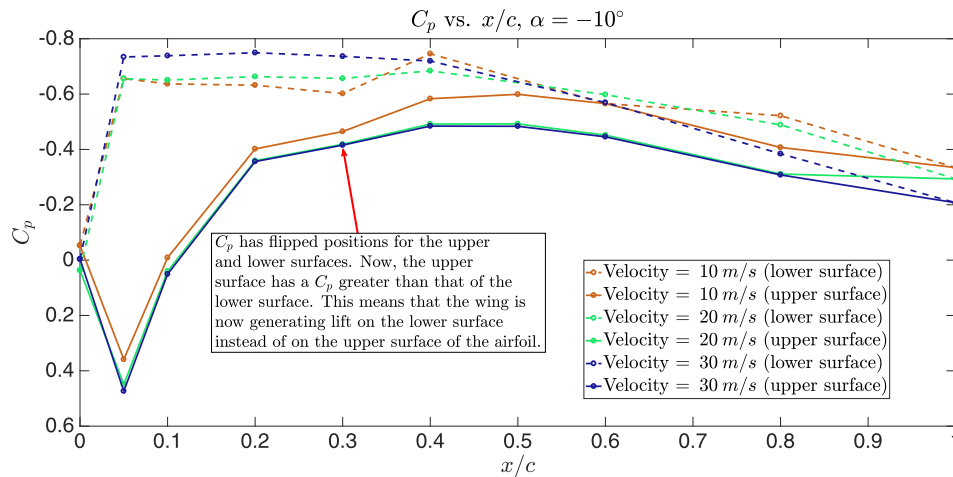


Figure 2: Plot Shows Pressure distribution over the airfoil at $\alpha = -10^\circ$

In Figures 2 - 4, one can view the pressure coefficient distributions at -10, 10, and 15 degrees angle of attack.

If one defines pressure difference as the difference between the pressure coefficients on the upper and lower surfaces of the airfoil it is clear to see that much can be learned about this pressure difference from Figures 2 - 4.

Firstly, it is worth noting that pressure difference in pressure distributions does not increase with increases in airspeed until the flow is within a close proximity of flow separation over the airfoil. If the flow is close to separation then an increase in airspeed helps to keep flow attached to the airfoil and therefore increases the pressure difference over the upper and lower surfaces. This is largely due to the increase in Reynolds number, which is the ratio of inertial to viscous forces in the flow. As the flow's velocity increases this ratio increases, and the increased inertia of the flow as compared to the viscous forces acting on it allows it to remain separated at higher angles of attack.

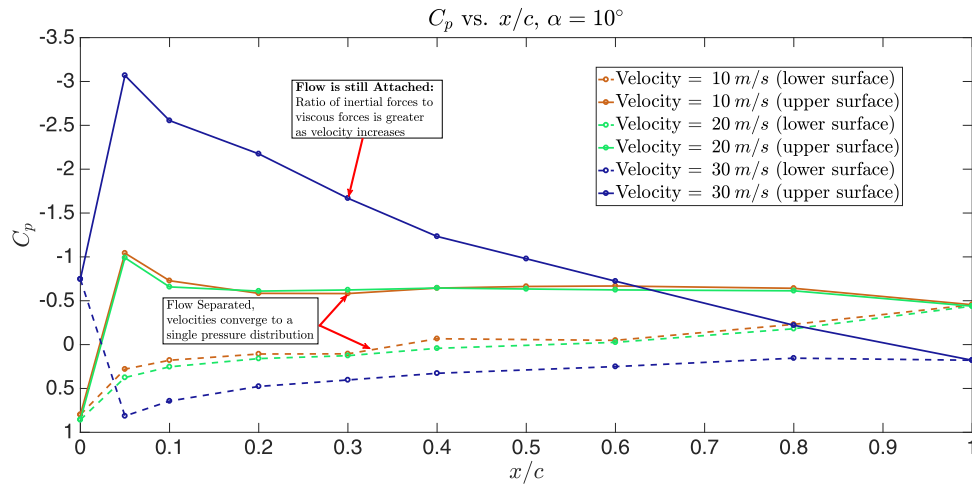


Figure 3: Plot Shows Pressure distribution over the airfoil at $\alpha = 10^\circ$

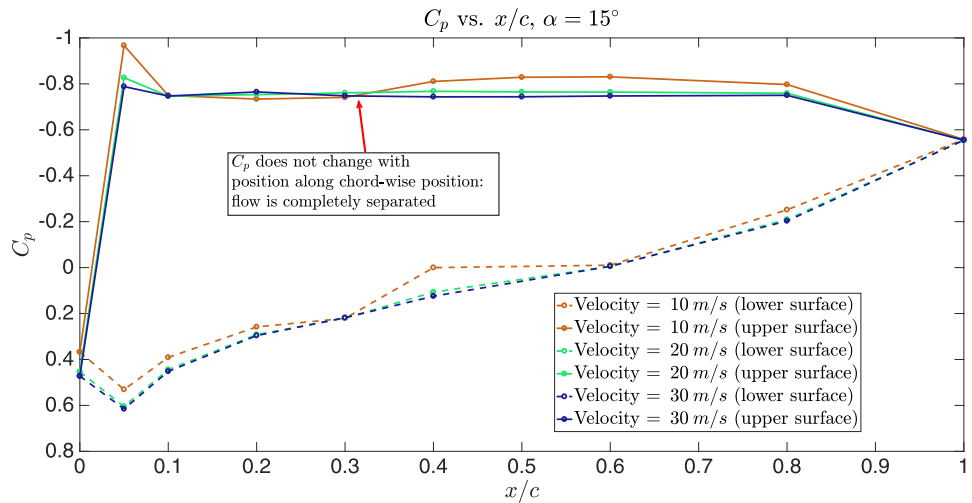


Figure 4: Plot Shows Pressure distribution over the airfoil at $\alpha = 15^\circ$

Next, examining low angles of attack where flow is attached, note that the pressure distributions remain similar as angle of attack changes. This is caused by the flow remaining attached to the airfoil which leads to stable pressure distributions. A comparison between a few small values of α can be seen in Figure 5. These plots show how at small values of α , the flow is steady and the C_p changes very little.

Also note that the largest pressure difference on the airfoil occurs before the quarter chord position in all plots. This means that the Clark Y-14 will have a pitching moment that makes the airfoil pitch to positive angles of attack.

Finally, note the difference between pressure coefficients at flow speed of 10 and 20 [m/s] and the pressure coefficients at flow speed of 30 [m/s] in Figure 3. Here, one can see that the pressure coefficients at 30 [m/s] are changing with respect to the shape of the airfoil over the total length of the cord. However at 10 and 20 [m/s] the pressure coefficients remain constant after a certain point on the cord. This means that for the lower velocities, C_p no longer is dependent on the shape of the airfoil and must not be flowing smoothly over the surface; the flow instead is defined by unsteady vortices along the surface. However, for the 30 [m/s] flow, C_p is changing with x/c and thus must still be allowing the surface to change its velocity - thus the flow is still attached. It can also be seen that pressure differences decrease over the airfoil as chord position increases.

As x/c approaches c , the pressure gradient drops, with the C_p on the upper surface increasing and C_p on the bottom surface decreasing. This means that there is a smaller pressure differential between the bottom and top of the airfoil, which means the flow is slowing down as it goes along the airfoil. This is indicative of an adverse pressure gradient, as flow is less and less willing to accelerate towards the end of the airfoil.

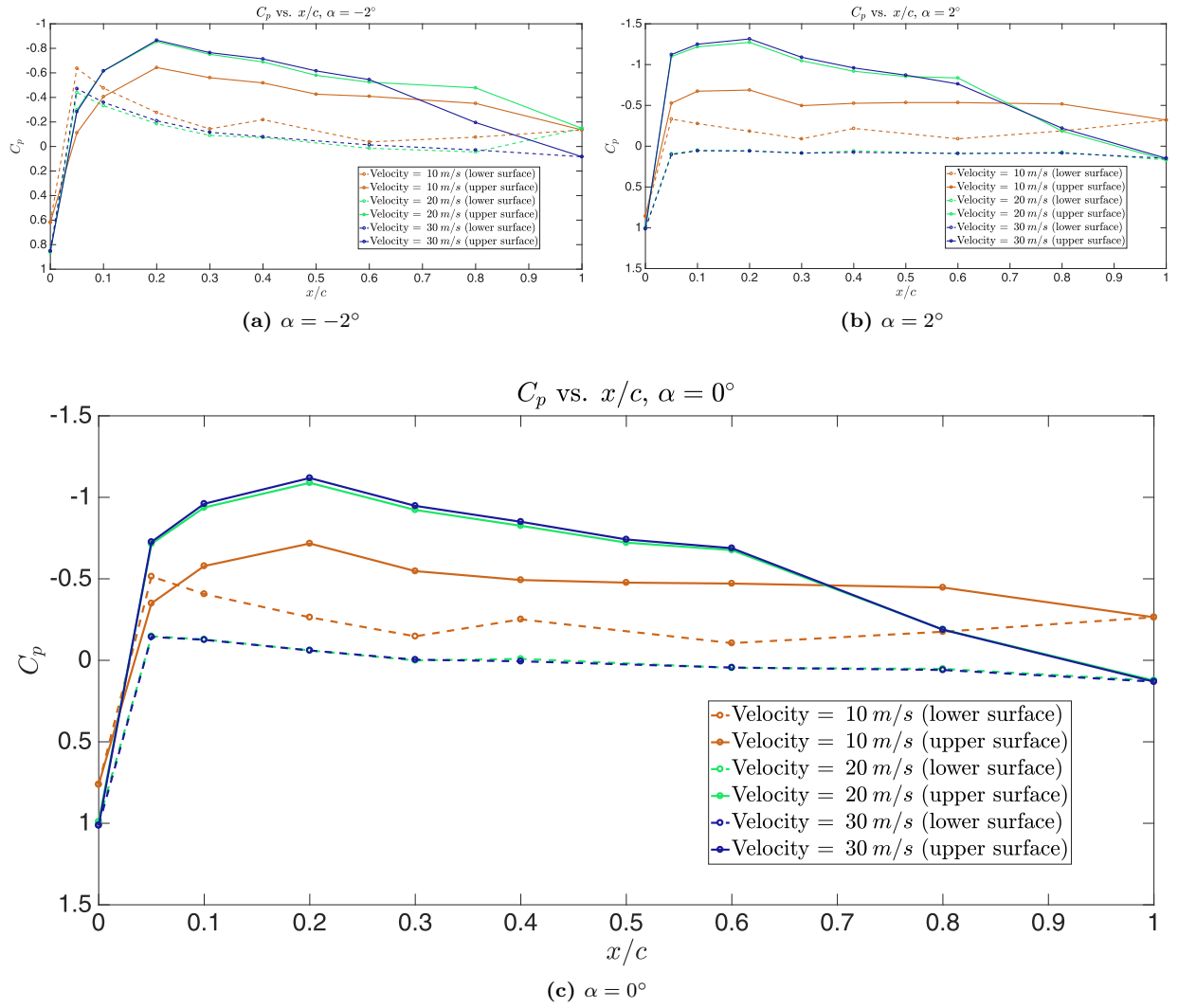


Figure 5: Plots showing how small changes to α (when α is small) affect C_p .

V. Lift and Pressure Drag Coefficients

In order to calculate lift and pressure drag, the pressure distribution must be integrated using numerical integration. In this investigation, the integration was performed using the axial forces (n and a) and then were converted to L and D which are defined relative to the flow. When defining the normal and axial forces over the i^{th} segment of the airfoil, the equations 6 and 7 are used.

$$n_i = -\frac{1}{2}(p_i + p_{i+1})\Delta x_i \quad (6)$$

$$a_i = \frac{1}{2}(p_i + p_{i+1})\Delta y_i \quad (7)$$

By identifying the pressure distribution along the upper and lower surfaces of the airfoil, the net forces perpendicular and parallel to the airflow (lift and pressure drag) can be determined. A comparison of the lift and pressure drag at varying air speeds shows how airspeed influences separation and stalling tendencies of the airfoil. With small angles of attack, the normal force influences lift the most while the axial force influences drag.

$$C_l = \frac{l}{\frac{1}{2}\rho_\infty V_\infty^2 c} = \frac{l}{q_\infty c} \quad (8)$$

$$C_d = \frac{d}{\frac{1}{2}\rho_\infty V_\infty^2 c} = \frac{d}{q_\infty c} \quad (9)$$

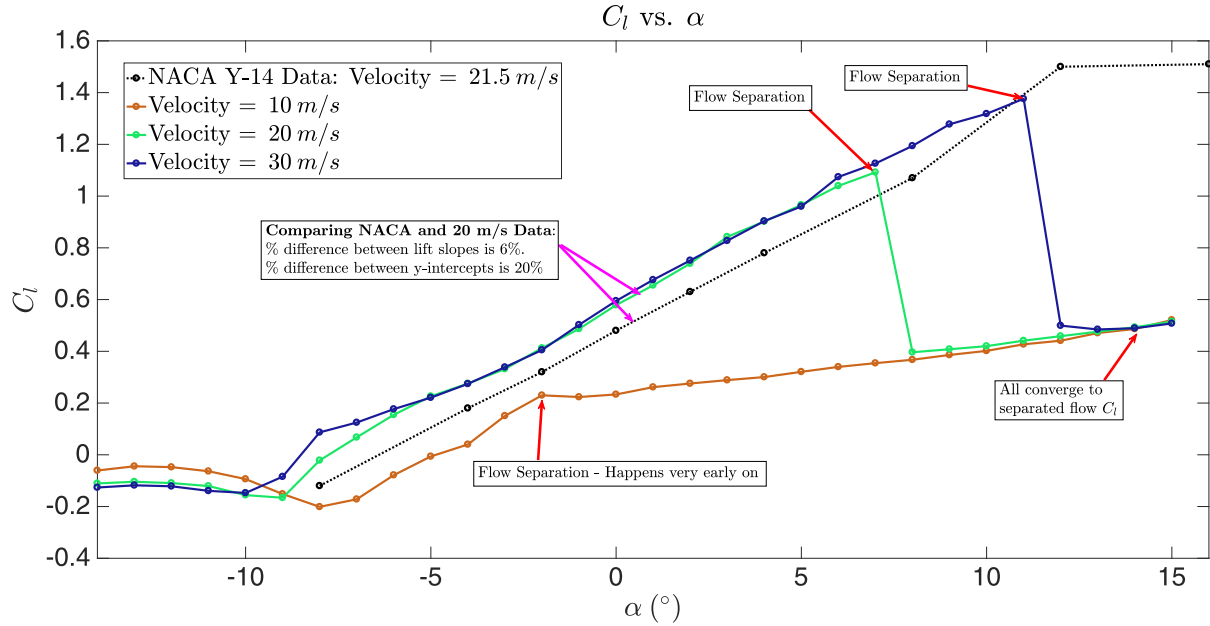


Figure 6: A plot of C_l vs. α , with annotations describing the many features of the plot

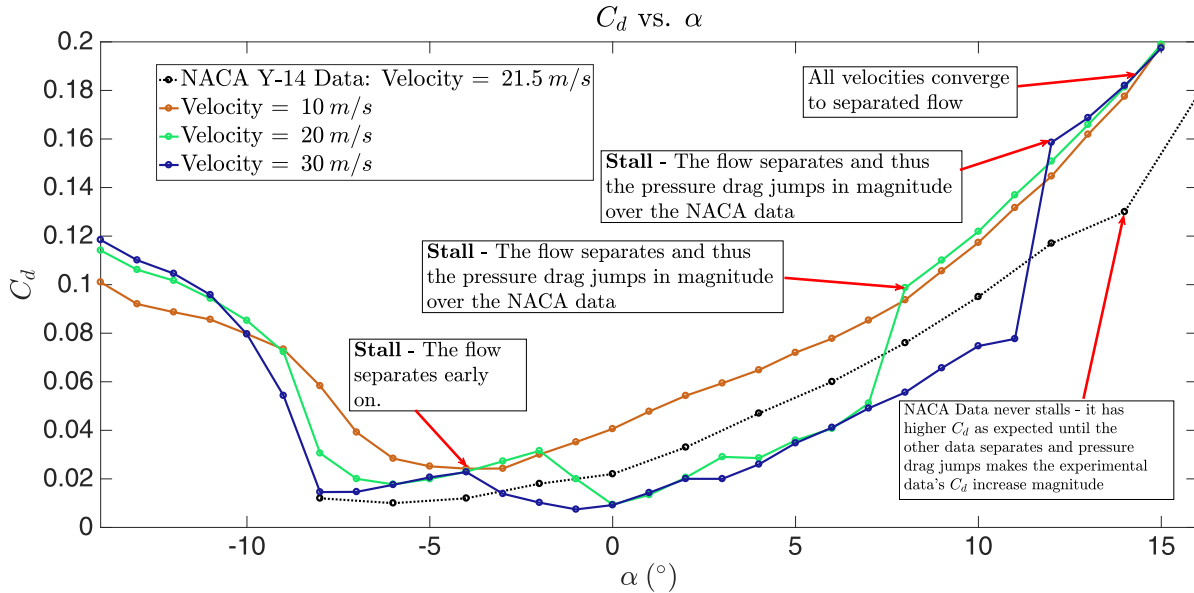


Figure 7: A plot of C_d vs. α

As shown in Figure 6, lift increases as angle of attack increases, as long as the flow has not separated. Additionally pressure drag decreases as the magnitude of angle of attack decreases, as long as the flow has not separated from the airfoil as seen in Figure 7. If flow has separated, pressure drag will increase drastically and lift will decrease drastically. The airfoil experiences sharp leading edge stall when the flow separates as seen in Section IV. As discussed before, the flow separation is dependent on Reynolds number (which is affected by flow speed) as well as angle of attack.

Next, note that the maximum lift coefficient the airfoil can generate is 1.376 and occurs at 11 degrees angle of attack as can be seen in Figure 6. This lift coefficient does vary with flow velocity as a higher flow

velocity leads to a higher Reynolds number. With a greater Reynolds number, a higher angle of attack can be achieved before flow separation occurs - finally resulting in a higher lift coefficient.

It is now worth mentioning that the lift coefficient produced at an angle of attack of zero degrees is between 0.2 and 0.6 depending on Reynolds number. Note that this lift coefficient is greater than zero as the airfoil is cambered and thus will instead produce a lift coefficient of zero at an angle of attack between -5 and -9 degrees depending on Reynolds number. Please view Figure 6 to visualize this phenomena.

Viewing Figure 6 it can be seen that the experimental data obtained for this lab is very similar to the data provided by NACA Technical Report #628, especially in the linear lift slope region. Note that the point of flow separation is later for the NACA data than the comparable lab data at flow velocity of 20 [m/s]. This inconsistency is most likely due to a variation in Reynolds number between the NACA data, which is measured at 21.5 [m/s], and the lab data, which is measured at 20 [m/s]. In addition the inconsistency in data fit can be explained by the conservation of mass principle. As α increases, the small size of the test section leads to the flow being compressed as it squeezes around the airfoil and the wall. Effectively, at higher angles of attack, the flow area around the airfoil decreases. This large decrease in cross-sectional area, combined with the sizable boundary layers that grow on the test section walls means that the flow is accelerated around the wing at higher angles of attack by the principle of conservation of mass. The flow area decreases, thus the flow velocity must increase. As the pressure distribution is directly related to the velocity over the wing by Equation 5, erroneously large velocities lead to erroneous values of C_l and C_d .

These inaccuracies contribute to the resultant inaccuracy between NACA and experimental data as seen in Figure 6, where one can see that the y-intercept inaccuracy is 20% and the slope inaccuracy is only 6%. To account for this, a simple correction factor of 0.12 can be applied. This correction factor is determined by comparing the angle of attack where the lab data reaches zero lift, and finding the C_l at this point in the NACA data. By determining the y-axis difference (lift coefficient value) between these points, the correction factor is achieved. Then, the lab data can be reduced by this correction factor and thus corrected to match much more closely in both its lift slope and in its C_l values at each α .

VI. Conclusion

This investigation of the Clark Y-14 airfoil has shown that the pressure distribution over an airfoil directly affects the lift force produced by an airfoil. The pressure distribution at varying angles of attack was plotted to show that as angle of attack is increased from zero, the C_l increases up until the flow separates from the airfoil surface. From the pressure distribution, the lift and pressure drag were calculated to demonstrate how these quantities vary with angle of attack. However, both of these quantities were calculated solely from integrating the pressure distribution around the airfoil surface. Lift arises almost entirely from this pressure distribution, as does pressure drag.

While in this lab we measured *pressure* drag, we did not take into account the viscous effects that make up a significant portion of the total drag C_d on the Clark Y-14 airfoil. This would mean that the data collected in this lab should have a smaller C_d at a similar α as compared to data that included the viscous effects on drag. The NACA data does take into account these effects, and as such is a good reference to compare our results with. This is not the trend demonstrated in Figure 7, and might be explained by the much higher Reynolds number used in the NACA tests which allows their airfoil to not stall as early as in our tests. As seen in Figure 7, when our data is not stalled, it follows the expected trend of having a lower C_d than the NACA data. Eventually, due to the lower Reynolds number used in our testing, we see stall in the airfoil data (Figures 6 & 7) which leads to greatly increased pressure drag on our airfoils. This huge jump in pressure drag overcomes the neglected friction drag, and makes our data have much greater C_d . The difference in testing conditions, combined with the quoted uncertainties in the pressure transducers can reasonably explain the differences between the NACA and our experimental data on the Clark Y-14 airfoil.

When comparing the C_l found in our lab to the NACA data, we find our measurements to very closely resemble those taken by NACA. The differences we see are likely caused by differences in measurement devices and by the different Reynolds numbers used in NACA measurements. The airfoil was also determined to have leading-edge stall characteristics. These findings are imperative to understanding two-dimensional flow around an airfoil and how lift and drag change related to angle of attack and flow velocity.